Optimum design of double-layer target for proton acceleration by ultrahigh intense femtosecond lasers considering relativistic rising edge

Masayasu Hata [*]

Kansai Institute for Photon Science (KPSI), National Institutes for Quantum Science and Technology (QST), Kizugawa, Kyoto 619-0215, Japan

Takayoshi Sano, Natsumi Iwata, and Yasuhiko Sentoku

Institute of Laser Engineering, Osaka University, Suita, Osaka 565-0871, Japan

Advances in laser technology have led to ever-increasing laser intensities. As a result, in addition to the amplified spontaneous emission and pedestal, it has become necessary to accurately treat the relativistic rising edge component. This component has not needed much consideration in the past because of its not relativistic intensity. In the previous study, a thin contamination layer was blown away from the target by the rear sheath field due to the relativistic rising edge component, and the target bulk was accelerated by the sheath field due to the main pulse. These indicated that the proton acceleration is not efficient in the target normal sheath acceleration by the ultrahigh intense femtosecond laser if the proton-containing layer is as thin as the contamination layer. Here we employ a double-layer target, making the second (rear) layer thick enough not to be blown away by the rising edge, so that the second layer is accelerated by the main pulse. The first layer is composed of heavy ions to reduce the total thickness of the target for efficient proton acceleration. We investigate an optimal design of a double-layer target for proton acceleration by the ultrahigh intense femtosecond laser considering the relativistic rising edge using two-dimensional particle-in-cell simulations. We also discuss how to optimize the design of such a double-layer target and find that it can be designed with two conditions: the first layer is not penetrated by hole boring, and the second layer is not blown away by the rising edge.

I. INTRODUCTION

The interaction of ultra-intense lasers with solids has a variety of applications including energetic ion and x-ray sources [1,2], radiography using charged particles or neutrons [3–7], fast ignition inertial confinement fusion [8–10], and material science [11,12]. In terms of medical applications, laser ion acceleration has attracted attention in hadron therapy and is being studied intensively [13,14]. Although there are various acceleration mechanisms for laser-accelerated ions, target normal sheath acceleration (TNSA) is the most simple and robust process [2,15–17]. Laser-accelerated ions in TNSA have many preferable characteristics for practical applications such as short pulses, point sources, and low emittance. Furthermore, laser accelerators have the potential to reduce the size and cost of conventional accelerators.

Due to the development of laser technology, as exemplified by chirped pulse amplification [18], the intensity of modern laser devices has reached around 10^{22} W/cm^2 [19–23]. In high-intensity lasers, the prepulse component at the rising edge significantly affects the main pulse interaction [24]. In our previous study [24], it was found that the presence of the rising edge prepulse component causes the efficient acceleration of silver ions in the silver target by the main pulse because the relativistic rising edge component preaccelerates and removes the contaminant layer on the target surface, and the silver target itself is directly exposed to the strong sheath electric field created by the main pulse. The rising edge prepulse component also affects various acceleration mechanisms, so optimal conditions need to be reconsidered. Pulse cleaning by plasma mirrors is essential to achieve ideal acceleration in ultrathin targets [25,26], and how cleanly the rising edge component can be removed is also important. On the other hand, changes in the waveform and spatial profile of the main pulse due to plasma mirrors may cause different problems.

This study discusses the optimal design for the proton acceleration target by considering the relativistic rising edge. In the previous study [24], silver ions in a silver film target were efficiently accelerated by detaching the proton-containing contamination layer due to the rising edge. However, if the proton-containing contamination layer is thicker, it is expected that protons rather than silver ions will be accelerated predominantly. So we consider a thicker proton-containing layer-coated target for efficient proton acceleration. Therefore, we will use a double-layer target with a proton layer coated on a silver thin film to evaluate the optimum thickness for efficient proton acceleration. The reason for using a silver thin film is that the total thickness of the target can be reduced. A thinner target can enhance the number fraction of hot electrons by electron circulation [27–29]. By using a large Z material, it is possible to reduce the thickness while

---

[*]hata.masayasu@qst.go.jp

maintaining a large areal density. In addition, the double-layer target is easy to understand because the generation of electrons by the interaction between the laser and the first layer is basically the same even if the material of the second (accelerated) layer is changed. If the target is too thin, the acceleration mechanism will change to radiation pressure acceleration and/or relativistic induced transparency [17,30–33], and the characteristics of the accelerated ions will change significantly. In this paper we focus on the TNSA regime with a moderate-thickness double-layer target.

The paper is organized as follows. In the next section, we describe the simulation method and discuss the numerical results for varying the thickness of the proton layer. In Sec. III we discuss the optimization of target design for TNSA acceleration using a double-layered target. Then we provide theoretical guidelines on how to determine the optimal proton layer thickness depending on the parameters of the relativistic rising edge and the thickness of the first layer to maintain TNSA. Section IV summarizes our conclusion.

II. SIMULATIONS

In this section we simulate proton acceleration by TNSA with a double-layer target. The thickness dependence of the second layer, i.e., the acceleration layer, is investigated to determine the optimum thickness.

A. Simulation setup

A double-layer target consisting of a silver thin film on the laser-irradiated side and a deuterium-hydrogen (DH) layer on the reverse side is employed. Here DH is mimicking CH simply for the reduction of computational cost. The thickness of the silver layer is fixed at 500 nm, and the thickness of the DH layer is varied to optimize the proton acceleration. The silver layer thickness is determined so that the laser does not penetrate the silver layer. The derivation of this thickness is described in Sec. III A.

In this analysis we fixed a laser condition based on the actual temporal profile [24] of the Japan-Kansai Advanced Relativistic Engineering Petawatt laser system (J-KAREN-P) that is the state-of-the-art ultrahigh intense femtosecond Ti:sapphire laser with the wavelength of $\lambda_L = 800$ nm. Figure 1(a) shows a cartoon of the whole temporal profile of the normalized laser intensity (see also Fig. 2 in Nishiuchi *et al.* [24] for the actual profile). The J-KAREN-P laser has lower-intensity long-pulse prepulse components called Amplified Spontaneous Emission (ASE) and pedestal. On the other hand, the relatively high-intensity subpicosecond prepulse component, called the rising edge, is arrived a just before the main pulse. The ASE has an intensity of around 10^{11} W/cm^2 over a timescale of hundreds ps, and the pedestal component increases gradually from 10^{11} to 10^{14} W/cm^2 at about 100 ps. The pulse duration of the main pulse is 40 fs, and the rising edge rises rather quickly from 10^{18} to 10^{20} W/cm^2 at about 400 fs. The peak intensity is set to 6×10^{21} W/cm^2, corresponding to a normalized vector potential $a_0 = eE_L/(m_e\omega_L c) = 53$, where e is the elementary charge, E_L and ω_L are the electric field amplitude and frequency of the laser, m_e is the electron mass, and c is the
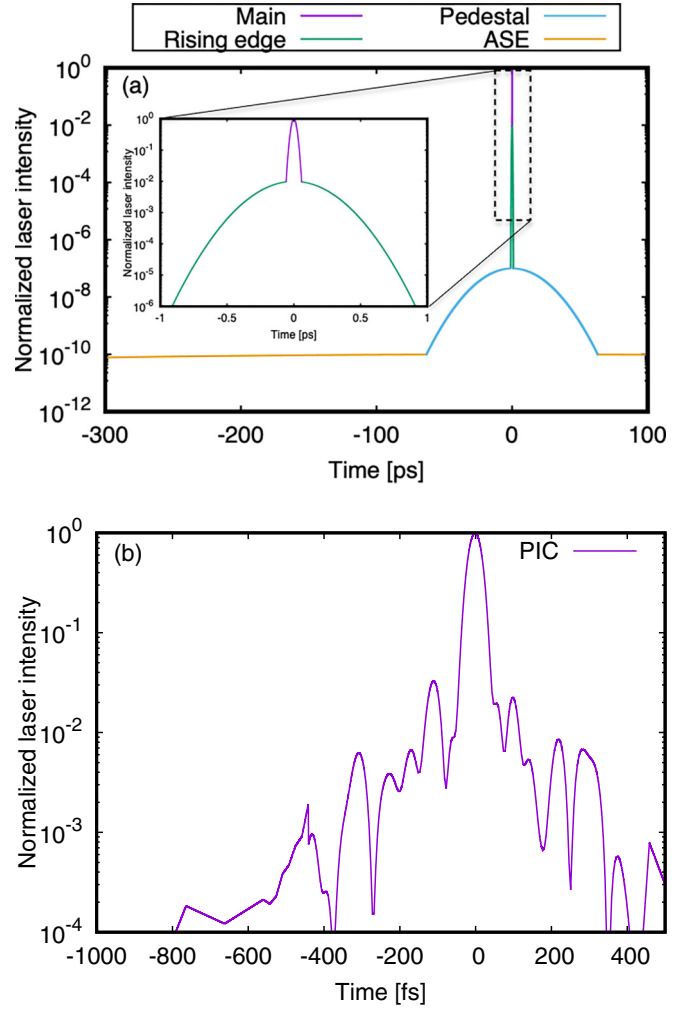

FIG. 1. (a) Cartoon of the J-KAREN-P laser temporal profile. The inset shows the zoomed region around the peak. (b) Actual laser temporal profile at $x = 0$ used in PIC simulations.

speed of light. The spot size was 2 μm diameter at $1/e^2$ laser intensity, and the laser incident angle to the target normal is $30°$. The laser light is assumed as the p polarization, namely, electric field oscillation in the 2D simulation plane to enhance the laser plasma interactions and hence TNSA compared to s polarization.

Since the laser intensity of the rising edge is one order of magnitude lower than that of the main pulse, a conventional laser (below 10^{20} W/cm^2) has an almost nonrelativistic rising edge, and the effect on the plasma is small. In contrast, since the intensity of the rising edge exceeds the relativistic intensity in the J-KAREN-P class laser, its effect cannot be ignored. Then the plasma interaction with the rising edge and main pulse is solved by a relativistic electromagnetic particle-in-cell (PIC) code. As the initial condition for the PIC simulations, we must assume the spatial distribution of the preplasma generated by the subnanosecond prepulse, namely, the ASE and pedestal. We obtained it from the corresponding hydrodynamic simulation, the same as in the previous work [24]. The fluid calculations show that the ASE and the pedestal cause the plasma to blow out from the front surface of
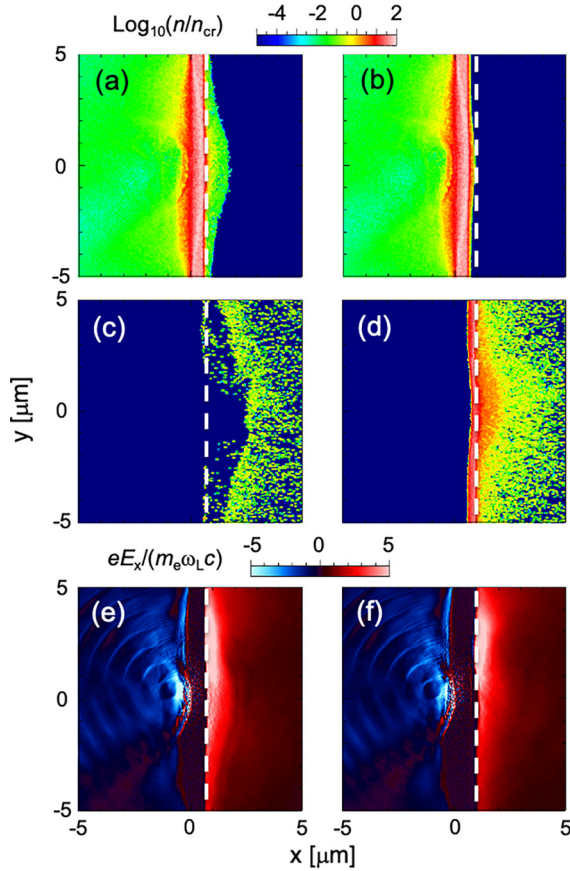
FIG. 2. Comparison between simulations with 10 nm (left column) and 200 nm DH layer thickness (right column); plotted are (a, b) silver and (c, d) proton density as well as (e, f) electric field along x. The white dotted lines are drawn at the starting position where the strong sheath field is generated.

the silver film, forming a preplasma. The size of the preplasma spread from the target surface was about 21 μm in the target normal direction and ±6 μm in the lateral direction up to an electron density of $0.01n_{cr}$. The preplasma scale length in the target normal direction was about 2 μm from $0.01n_{cr}$ to n_{cr} density and about 0.3 μm from n_{cr} to $500n_{cr}$. The average ionization degree of silver near the critical density was about 25.

We have conducted PIC simulations in a 2D Cartesian geometry using PICLS code which is a relativistic electromagnetic PIC code including collision with weighted particles and ionization due to field and collision [34]. The temporal profile of the normalized laser intensity used in PIC simulations is shown in Fig. 1(b). It includes the main pulse and rising edge components. The surface of the original target was set to $x = 0$, and the focus point of the laser was taken as the origin $(x, y) = (0, 0)$ (see Fig. 2). The laser is irradiated onto the target from the negative x and negative y directions with the incidence angle to the target normal of 30°. The time at which the peak of the main pulse reaches the original target surface $x = 0$ is defined as $t = 0$. The size of the simulation box was $-20 \leqslant x \leqslant 40$ μm and $-30 \leqslant y \leqslant 30$ μm. The sizes of the grid and time step are set to 10 nm and 33.4 as, respectively. We adopt the absorbing boundary condition for the

electromagnetic fields and the reflection boundary condition for particles except for fast electrons with a Lorentz factor of more than 2. These fast electrons are absorbed at the boundary because they rarely return in the simulation time In the PIC calculations, the initial profiles of density and charge state of the silver layer were introduced from the hydro calculation mentioned above, while the plasma temperature was set to zero, as the initial temperature is insignificant compared to the final temperature. In the previous study, the thickness of the HD layer on the rear surface was fixed at 20 nm. In the present study, the thickness is varied from 10 to 5000 nm with an electron density of $100n_{cr}$. The number of silver ions per cell is 1, and each silver ion has 47 electrons. The numbers of H and D per cell are both five. The HD layer is completely ionized by relativistic laser interactions, so the same number of electrons are placed into the cell. We have adopted a fourth-order current/force interpolation to reduce the numerical heating.

B. Results

To see the thickness dependence of the second layer (DH), we compare two typical cases, one with a thickness of 10 nm and the other with a thickness of 200 nm. Figure 2 shows the spatial profiles of [Figs. 2(a) and 2(b)] silver ion and [Figs. 2(c) and 2(d)] proton number density and [Figs. 2(e) and 2(f)] the laser cycle averaged electric field normal to the target E_x at the laser peak irradiation timing of $t = 0$ for the second layer thicknesses of [Figs. 2(a), 2(c), and 2(e)] 10 nm and [Figs. 2(b), 2(d), and 2(f)] 200 nm, respectively. The white dotted lines indicate the peak position of the strong sheath field, which means the ion acceleration site.

A comparison of the silver density profiles shows that in both cases the silver plasma is pushed by the hole boring due to the main pulse. The initial silver plasma profiles are based on the same hydrodynamic calculations, so the interaction at the front surface proceeds in a similar manner for both cases. On the other hand, the situation on the backside is completely different. For the case of 10 nm-DH, the silver on the backside expands, whereas almost no silver expansion occurs in the case of 200 nm.

Obvious differences can be seen also in the proton density profiles. In the 10 nm case, the rising edge blows off the proton layer on the order of μm before the main pulse arrival, while the second layer is not blown off entirely in the 200 nm case. Although the rising edge accelerates the protons in advance, the proton layer remains in contact with the high-density silver layer even after the main pulse arrives. This indicates that in the case of 10 nm, the second layer is peeled off by the rising edge, and as a result, the silver is pre-expanded. In the case of 200 nm, the proton layer remains enough after the rising edge irradiation to prevent the silver from expanding.

The average electric field profile shows that a strong sheath electric field is generated by fast electrons accelerated by the main pulse irradiation and ejected from the back surface. The sheath electric field on the back surface reached a maximum of over 30 TV/m. Only ions in the sheath electric field generated by the main pulse irradiation are accelerated significantly. In fact, for the 10 nm case, there are almost no protons, and a large number of silver ions are present at the

sheath generation point. In contrast, for the 200 nm case, the bulk of protons remains firmly at the sheath generation point and silver is absent. Therefore, it is expected that silver is efficiently accelerated in the case of 10 nm, and protons are efficiently accelerated in the case of 200 nm.

For thicker targets, the same trend is found as in the 200 nm case. Even in the 5000 nm case, the thickest target in our simulations, the efficient proton acceleration occurs, with no peeling off of the second layer due to the rising edge and a sufficient amount of protons remaining in contact with the silver, so that no silver expansion occurs and a strong sheath is generated in the second layer.

Figure 3 shows the energy spectrum of each ion for the second layer thicknesses of [Fig. 3(a)] 10, [Fig. 3(b)] 200, and [Fig. 3(c)] 5000 nm. Here the observation region is $x \geqslant$ 1 μm, and only ions accelerated in the x-positive direction are measured. It means that the component of the front silver acceleration is excluded, and only rear acceleration, namely TNSA is focused on. The silver ions are accelerated by the hole-boring process at the front surface, but it does not reach the rear surface in these simulations. The detailed silver ion acceleration characteristics are discussed in previous research [24]. The observation time of $t = +360$ fs is the time just before the fastest proton reached the boundary of $x = 40$ μm. The maximum ion energy is the highest in the case of 200 nm, and it exceeds 100 MeV/u, an increase of about 50% in maximum energy compared to the 10 nm target. As in the previous study, we confirm that silver is accelerated when the second layer is sufficiently thin. When the second layer is thicker (5000 nm), silver ions are not accelerated. In addition, the proton acceleration is weaker than that of the 200 nm case, and the maximum energy is reduced by about 20%. This is thought to be due to the thicker target, which reduces the density of the fast electron flow emitted from the back surface, resulting in a reduced sheath. It is noted that this effect might be more pronounced in the three-dimensional space.

Based on these results, an optimal thickness for the second layer should exist, so additional simulations have been performed. The thickness dependence of the second layer on the maximum energy of each ion is shown in Fig. 4. The maximum proton energy is 73 MeV for the 10 nm case and reaches a maximum of 106 MeV for the 200 nm case. As the second layer became thicker beyond 200 nm, the energy drops to 84 MeV. On the other hand, the maximum energy of silver is 20 MeV/u for the 10 nm case and decreases monotonically with increasing thickness of the second layer to 0.27 MeV/u for the 5000 nm case. The maximum energy of the deuteron is 23 MeV for the 10 nm case and almost independent of increasing the thickness of the second layer. The deuterons are initially accelerated by the strong sheath field, but after a while the protons take precedence and the deuterons hardly feel the strong sheath field. Since the deuterons initially exist at the rear surface, they are accelerated for all cases despite the second layer thickness. These results indicate that the thickness of the second layer should be selected to be thicker than 50 nm and thinner than 1000 nm, which is suitable for proton acceleration. Instead, if we want to accelerate silver, the second layer should be removed as thin as possible.

Due to particle number limitations and statistical errors, it may be premature to determine the optimal parameters based
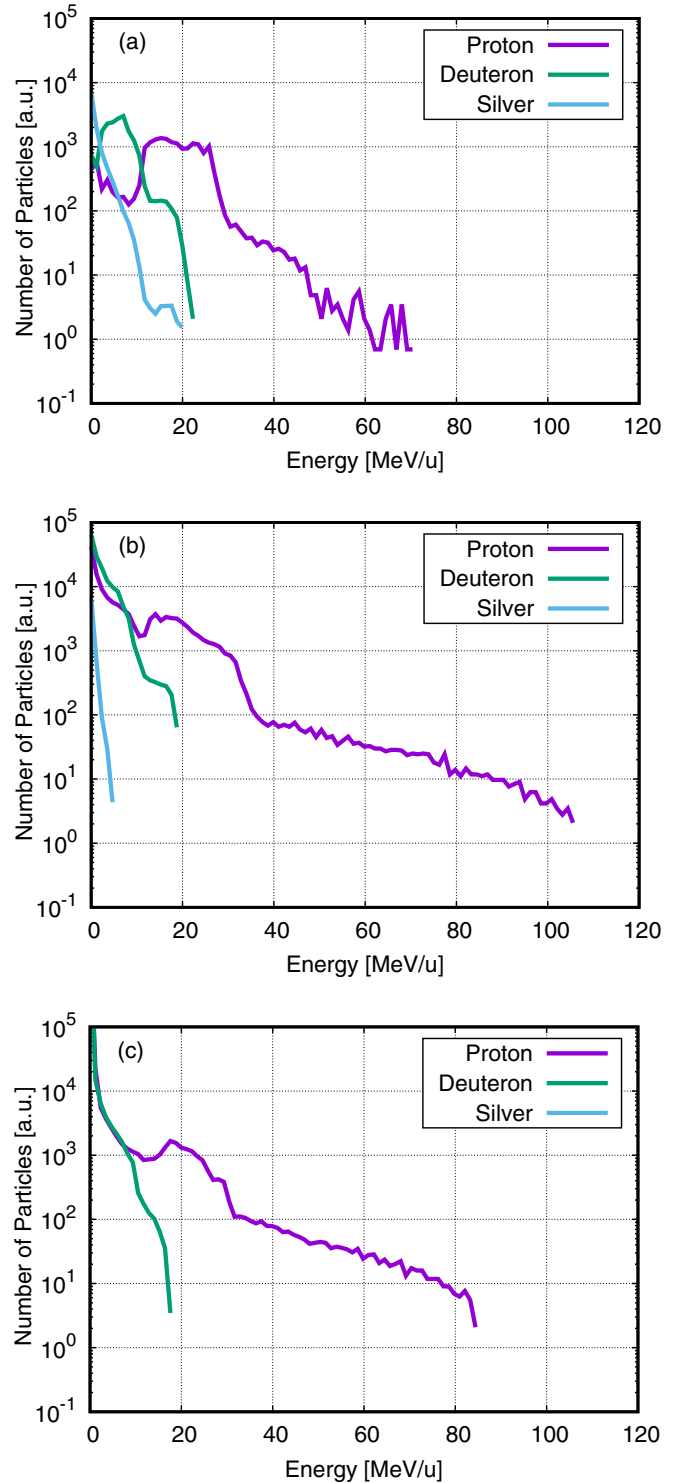

FIG. 3. Energy spectra of rear accelerated ions at +360 fs after the laser peak irradiation in the cases of (a) 10, (b) 200, and (c) 5000 nm, where each color indicates an ion species.

on the maximum ion energies alone. Therefore, we investigate the optimal thickness in terms of the number of accelerated protons above a certain energy. Figure 5 shows the dependence of the number of protons above 30, 60, and 90 MeV on the thickness of the second layer. This result indicates that a thickness of about 200 nm is suitable for high-energy proton
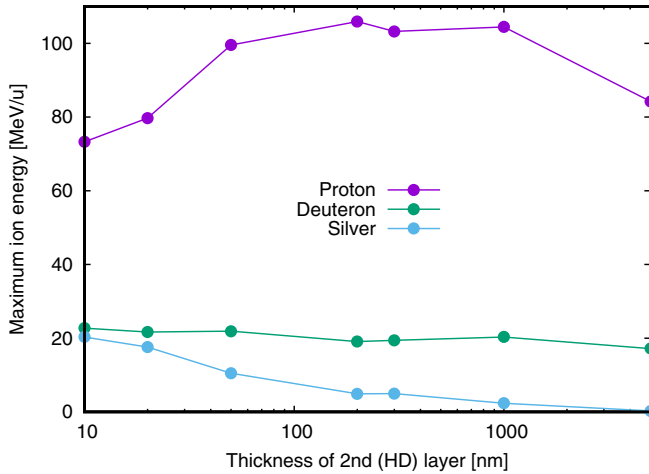
FIG. 4. Maximum ion energy against the second layer thickness. Each color indicates an ion species.

FIG. 6. Dependence of the laser absorption rate and energy coupling efficiency from laser to ions on the thickness of the second layer just before the fastest proton reached the boundary.

acceleration in terms of the number of high-energy protons generated.

In addition, we also investigate the laser absorption rate and energy coupling efficiency from laser to ions just before the fastest proton reached the boundary, namely, at 360 fs after the laser peak irradiation, as shown in Fig. 6. Owing to the same first layer, laser absorption rates are almost the same for all simulations. The coupling efficiency from the laser to silver ions becomes high with decreasing the second layer thickness. Energy coupling efficiencies from laser to protons and deuterons have a peak around the second layer thickness of 200 or 300 nm. For the thinner second layer case, the coupling efficiency to the protons is reduced by the detachment effect of the rising edge, and the acceleration of silver is improved. On the other hand, for the thicker second layer case, the reduction of the sheath fields due to the thickness reduces the coupling efficiency to protons and deuterons and

prevents the second layer from blowing away, so the coupling efficiency to silver does not change because the acceleration on the laser-irradiated surface side is dominant. These results are also consistent with the above results.

III. DISCUSSION

In this section we discuss the optimization of target design for TNSA acceleration using a double-layered target. It is assumed that the material in the second layer is light ions. When the ultrahigh intense laser shoots a thin material composed of light ions, it will be penetrated, and TNSA will not be established. Therefore, by employing a double-layered target, a material composed of heavy ions is placed on the irradiation side of the target to prevent penetration of the laser and to allow TNSA to accelerate the second layer namely the acceleration layer. The advantage of this method is that the efficiency of TNSA acceleration can be increased by using heavy ions in the first layer to make the whole target thickness thinner.

In order to establish TNSA with a double-layered target, it is essential that (1) the first layer is not penetrated by the main pulse hole boring and (2) the second layer is not detached by the rising edge. In the following subsections, these two conditions will be discussed.
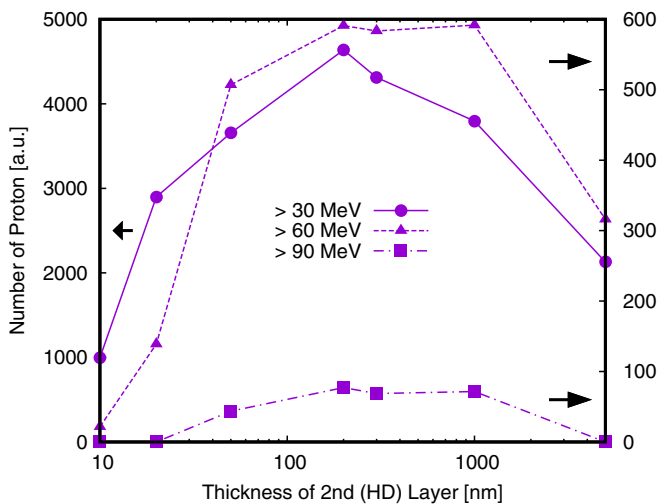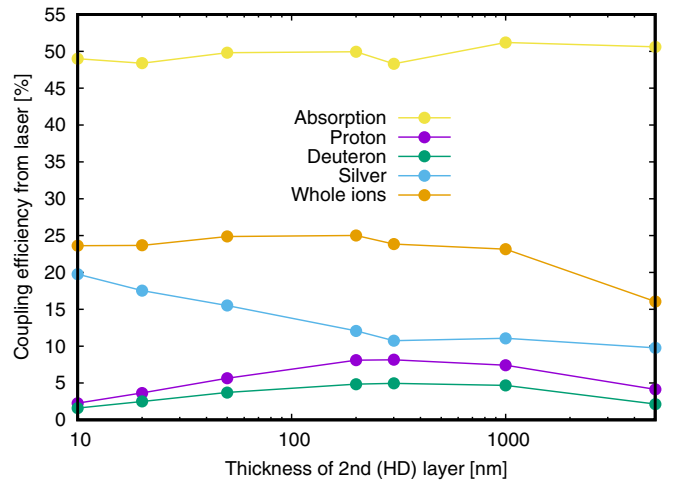

FIG. 5. Dependence of the number of protons above 30, 60, and 90 MeV on the thickness of the second layer. The number of protons above 30 MeV is shown on the left axis and the others on the right axis.

A. No penetration of the heavy ion layer (first layer) by the main pulse hole boring

We consider how much the thickness of the first layer can be reduced. A high-intensity laser has a large radiation (photon) pressure that can push the plasma away and dig a hole. This phenomenon is well known as hole boring, and its speed can be obtained from the pressure balance equation [35]

$$(1 + R)\frac{I}{c} = n_e T_e + 2n_i M_i v_{HB}^2, \qquad (1)$$

where R is the reflectivity, I is the laser intensity, c is the speed of light, n_e, T_e, and n_i are the electron density, electron temperature and ion density at the interaction surface, M_i is the

ion mass, and v_{HB} is the hole-boring speed. The left-hand side is the radiation pressure, the first term on the right-hand side is the electron pressure, and the second term is the dynamic pressure of the ions. In calculating the dynamic pressure, we used the relationship that the velocity of ions pushed by the light pressure is approximately twice that of the hole boring. The unreflected laser component is absorbed and converted to an electron energy density flux. The electron pressure can be obtained from the following equation of the energy flux conservation:

$$(1 - R)I = n_e T_e v_e \sim n_e T_e c, \tag{2}$$

where the velocity in the electron flux term is approximated to be the speed of light because we are considering a relativistic laser. Eliminating the electron pressure term from Eq. (1) using Eq. (2), the hole-boring velocity is $v_{HB} = (RI/M_i n_i c)^{1/2} = ca_0 (Rm_e n_c / 2M_i n_i)^{1/2}$. Since TNSA acceleration is employed as the acceleration mechanism in this paper, the first layer must not be broken by this hole boring. Therefore, the following conditions are imposed using the hole-boring velocity

$$L_1 > L_{HB} \equiv v_{HB}\tau = \lambda_L \frac{\tau}{\tau_L} a_0 \left(\frac{R m_e n_c}{2 M_{i1} n_{i1}} \right)^{1/2}, \tag{3}$$

where L_1, M_{i1}, n_{i1} is the thickness, ion mass, and ion density of the first layer, and τ_L and τ are the laser period and acceleration time, or pulse duration, respectively. The reflectivity is difficult to evaluate accurately because it varies over time depending on a variety of factors, including plasma profile, laser intensity, and polarization. Therefore, the most stringent conditions are adopted by substituting the maximum velocity at the perfect reflection as the hole-boring velocity. By substituting the conditions of the present simulation ($\tau = 15.0\tau_L$, $a_0 = 53.03$, $\lambda_L = 800$ nm, $n_{i1} = 58.5n_c$, $M_{i1} = 107.9M_p$, $M_p = 1836m_e$), the required first layer thickness is determined to be 132 nm or more. According to previous studies [24], simulations and experiments with a silver thickness of 50 nm have shown that the silver film breaks and strong transmission of laser light occurs, suggesting that this estimate is reasonable. If we apply this calculation to light ions, e.g. carbon, we obtain $M_{i1} = 12.01M_p$, and assuming little difference in ion number density, $L_{HB} \sim 395$ nm. Therefore, we can see that the thickness can be reduced to less than one-third by using a heavy element such as silver. In fact, simulations confirm that even 200 nm silver does not penetrate. In reality, however, it is necessary to consider the effects of ASEs, pedestals, and rising edges, so a silver film of 500 nm, the same thickness as in the experiment, was used in the series of simulations as a sufficiently tolerable thickness.

B. No detachment of the accelerated light ion layer (second layer) during the rising edge interactions

The detachment of the second layer can be discussed by one-dimensional expansion in the vicinity of the laser spot [see Fig. 2(c)]. Assuming that a second layer of HD plasma of ion density n_{i2} and thickness L_2 expands at the speed of sound by irradiation of a rising edge of relativistic

intensity $a_{rise} = 1$ from t_{rise} femtoseconds before the main pulse arrives, the thickness after expansion is $L_{2,after} = C_s t_{rise}$. Here the sound speed is expressed as $C_s = (ZT_2/M_i)^{1/2} = c[(\gamma_{rise} - 1)Z_2 m_e/M_i]^{1/2}$. The temperature of the second layer can be roughly estimated as the average energy of the return current by considering that the return current that cancels the fast electron flow relaxes due to collisions and two-fluid instabilities, i.e., $T_2 = n_c T_H/Z_2 n_{i2}$. The density of the second layer at the time of main pulse irradiation is estimated to be $n_{i2,after} \sim n_{i2}L_2/C_s t_{rise}$. In order to use the second layer as an acceleration layer, the sheath must stand up in the second layer, so the electron density must be kept above the fast electron flow density, i.e., $Z_2 n_{i2,after} > \gamma_{main}n_c$. Therefore, the following conditions are derived:

$$L_2 > \lambda_L \frac{\tau_{rise}}{\tau_L} \frac{\gamma_{main}n_c}{n_{i2}} \left[\frac{m_e}{Z_2^2 M_{i2}} \frac{n_c}{n_{i2}} (\gamma_{rise} - 1) \right]^{1/2}. \tag{4}$$

Substituting the parameters of the present simulation ($\tau = 150\tau_L$, $a_{rise} = 1$, $\lambda_L = 800$ nm, $n_{i2} = 50n_c$, $Z_2 = 2$, $M_{i1} = 1.5M_p$, $M_p = 1836m_e$), we obtain 102 nm, which is a good agreement because the proton acceleration efficiency is better above approximately this thickness. The discussion here has clarified the lower limit of the thickness of the second layer required for efficient proton acceleration, but what is the upper limit? In ion acceleration based on the TNSA, the thicker the target, the greater the divergence loss of the fast electron flow due to geometrical and collisional effects, so it is important to achieve quasi-one-dimensional sheath acceleration with as thin a target as possible. Therefore, the whole target thickness should be less than or equal to the spot diameter, i.e., about a micron under the laser conditions of this paper.

IV. SUMMARY

In this paper we focus on the relativistic rising edge that should be considered in recent ultra-intense femtosecond laser systems above 10^{21} W/cm^2 and clarify how to efficiently accelerate protons in TNSA acceleration using a double-layer target. In order to employ TNSA acceleration, this method (1) determines the thickness of the first layer so that the target is not broken by the hole boring of the main pulse and (2) ensures that the second layer, which is the acceleration layer, is not stripped by the rising edge before the main pulse reaches it. The thickness of the second layer is determined so that the second layer, which is the acceleration layer, will not be entirely peeled by TNSA before the time the main pulse arrives.

Knowledge of the laser conditions, including the rising edge, makes it possible to determine the thicknesses of the first and second layers of the double-layer target using the above procedure. The optimum target conditions thus derived are in good agreement with the results of the optimum thickness of the second layer revealed by the two-dimensional PIC simulations. The three-dimensional effect is expected to be more pronounced in the reduction of the back-surface sheath field with target thickness, and the tolerance for the optimal thickness of the second layer in Fig. 3 is expected to be narrower on the thicker side.

The maximum energy and the absolute number of generated ions can be quantitatively evaluated for the first time by three-dimensional simulation, but this requires abundant computational resources and remains a challenge for the future. The proton energies used in cancer therapy range from 70 to 230 MeV. Laser energy must be increased to achieve high-energy proton acceleration to meet the requirements of cancer therapy. Dover *et al.* [36] found that if the laser intensity is increased too much at a small spot, the quiver amplitude of the electrons shaken by the laser exceeds the spot diameter, and the electrons are not efficiently accelerated. In the study by Takagi *et al.* [37], scaling including this effect is derived using Bayesian estimation, and it is shown that protons can be accelerated more efficiently by increasing the pulse width. Therefore, it is considered necessary to increase the laser intensity and pulse width while keeping the spot size above the quiver amplitude when increasing the

laser energy. These studies also remain as future research topics.

[1] H. Daido, M. Nishiuchi, and A. S. Pirozhkov, Rep. Prog. Phys. **75**, 056401 (2012).

[2] A. Macchi, M. Borghesi, and M. Passoni, Rev. Mod. Phys. **85**, 751 (2013).

[3] A. J. Mackinnon, P. K. Patel, R. P. Town, M. J. Edwards, T. Phillips, S. C. Lerner, D. W. Price, D. Hicks, M. H. Key, S. Hatchett *et al.*, Rev. Sci. Instrum. **75**, 3531 (2004).

[4] A. J. Mackinnon, P. K. Patel, M. Borghesi, R. C. Clarke, R. R. Freeman, H. Habara, S. P. Hatchett, D. Hey, D. G. Hicks, S. Kar *et al.*, Phys. Rev. Lett. **97**, 045001 (2006).

[5] C. K. Li, F. H. Séguin, J. A. Frenje, J. R. Rygg, R. D. Petrasso, R. P. J. Town, P. A. Amendt, S. P. Hatchett, O. L. Landen, A. J. Mackinnon *et al.*, Phys. Rev. Lett. **97**, 135003 (2006).

[6] D. P. Higginson, J. M. McNaney, D. C. Swift, T. Bartal, D. S. Hey, R. Kodama, S. Le Pape, A. Mackinnon, D. Mariscal, H. Nakamura *et al.*, Phys. Plasmas **17**, 100701 (2010).

[7] M. Zimmer, S. Scheuren, A. Kleinschmidt, N. Mitura, A. Tebartz, G. Schaumann, T. Abel, T. Ebert, M. Hesse, Ş. Zähter *et al.*, Nat. Commun. **13**, 1173 (2022).

[8] M. Tabak, J. Hammer, M. E. Glinsky, W. L. Kruer, S. C. Wilks, J. Woodworth, E. M. Campbell, M. D. Perry, and R. J. Mason, Phys. Plasmas **1**, 1626 (1994).

[9] R. Kodama, P. A. Norreys, K. Mima, A. E. Dangor, R. G. Evans, H. Fujita, Y. Kitagawa, K. Krushelnick, T. Miyakoshi, N. Miyanaga *et al.*, Nature (London) **412**, 798 (2001).

[10] M. Roth, T. E. Cowan, M. H. Key, S. P. Hatchett, C. Brown, W. Fountain, J. Johnson, D. M. Pennington, R. A. Snavely, S. C. Wilks *et al.*, Phys. Rev. Lett. **86**, 436 (2001).

[11] C. I. Blaga, J. Xu, A. D. DiChiara, E. Sistrunk, K. Zhang, P. Agostini, T. A. Miller, L. F. DiMauro, and C. D. Lin, Nature (London) **483**, 194 (2012).

[12] M. Barberio, M. Scisciò, S. Vallières, F. Cardelli, S. N. Chen, G. Famulari, T. Gangolf, G. Revet, A. Schiavi, M. Senzacqua, and P. Antici, Nat. Commun. **9**, 372 (2018).

[13] S. V. Bulanov, J. J. Wilkens, T. Z. Esirkepov, G. Korn, G. Kraft, S. D. Kraft, M. Molls, and V. S. Khoroshkov, Phys. Usp. **57**, 1149 (2014).

[14] F. Kroll, F.-E. Brack, C. Bernert, S. Bock, E. Bodenstein, K. Brüchner, T. E. Cowan, L. Gaus, R. Gebhardt, U. Helbig *et al.*, Nat. Phys. **18**, 316 (2022).

[15] R. A. Snavely, M. H. Key, S. P. Hatchett, T. E. Cowan, M. Roth, T. W. Phillips, M. A. Stoyer, E. A. Henry, T. C. Sangster, M. S. Singh *et al.*, Phys. Rev. Lett. **85**, 2945 (2000).

[16] M. Passoni, L. Bertagna, and A. Zani, New J. Phys. **12**, 045012 (2010).

[17] A. Macchi, A. Sgattoni, S. Sinigardi, M. Borghesi, and M. Passoni, Plasma Phys. Control. Fusion **55**, 124020 (2013).

[18] D. Strickland and G. Mourou, Opt. Commun. **56**, 219 (1985).

[19] A. S. Pirozhkov, Y. Fukuda, M. Nishiuchi, H. Kiriyama, A. Sagisaka, K. Ogura, M. Mori, M. Kishimoto, H. Sakaki, N. P. Dover *et al.*, Opt. Express **25**, 20486 (2017).

[20] H. Kiriyama, A. S. Pirozhkov, M. Nishiuchi, Y. Fukuda, K. Ogura, A. Sagisaka, Y. Miyasaka, M. Mori, H. Sakaki, N. P. Dover *et al.*, Opt. Lett. **43**, 2595 (2018).

[21] Nat. Mater. **15**, 1 (2016).

[22] K. A. Tanaka, K. M. Spohr, D. L. Balabanski, S. Balascuta, L. Capponi, M. O. Cernaianu, A. Cuciuc, A. Cucoanes, I. Dancus *et al.*, Matter Radiat. Extremes **5**, 024402 (2020).

[23] J. W. Yoon, Y. G. Kim, I. W. Choi, J. H. Sung, H. W. Lee, S. K. Lee, and C. H. Nam, Optica **8**, 630 (2021).

[24] M. Nishiuchi, N. P. Dover, M. Hata, H. Sakaki, K. Kondo, H. F. Lowe, T. Miyahara, H. Kiriyama, J. K. Koga, N. Iwata *et al.*, Phys. Rev. Res. **2**, 033081 (2020).

[25] H. C. Kapteyn, M. M. Murnane, A. Szoke, and R. W. Falcone, Opt. Lett. **16**, 490 (1991).

[26] A. Kon, M. Nishiuchi, Y. Fukuda, K. Kondo, K. Ogura, A. Sagisaka, Y. Miyasaka, N. P. Dover, M. Kando, A. S. Pirozhkov *et al.*, High Power Laser Sci. Eng. **10**, e25 (2022).

[27] Y. Sentoku, T. E. Cowan, A. Kemp, and H. Ruhl, Phys. Plasmas **10**, 2009 (2003).

[28] N. Iwata, K. Mima, Y. Sentoku, A. Yogo, H. Nagatomo, H. Nishimura, and H. Azechi, Phys. Plasmas **24**, 073111 (2017).

[29] N. Iwata, A. J. Kemp, S. C. Wilks, K. Mima, D. Mariscal, T. Ma, and Y. Sentoku, Phys. Rev. Res. **3**, 023193 (2021).

[30] V. A. Vshivkov, N. M. Naumova, F. Pegoraro, and S. V. Bulanov, Phys. Plasmas **5**, 2727 (1998).

[31] T. Esirkepov, M. Borghesi, S. V. Bulanov, G. Mourou, and T. Tajima, Phys. Rev. Lett. **92**, 175003 (2004).

[32] A. Macchi, A. Sgattoni, S. Sinigardi, M. Borghesi, and M. Passoni, Plasma Phys. Control. Fusion **56**, 039501 (2014).

[33] A. Higginson, R. J. Gray, M. King, R. J. Dance, S. D. R. Williamson, N. M. H. Butler, R. Wilson, R. Capdessus, C. Armstrong, J. S. Green *et al.*, Nat. Commun. **9**, 724 (2018).

[34] Y. Sentoku and A. J. Kemp, J. Comput. Phys. **227**, 6846 (2008).

[35] Y. Sentoku, W. Kruer, M. Matsuoka, and A. Pukhov, Fusion Sci. Technol. **49**, 278 (2006).

[36] N. P. Dover, M. Nishiuchi, H. Sakaki, K. Kondo, M. A. Alkhimova, A. Y. Faenov, M. Hata, N. Iwata, H. Kiriyama, J. K. Koga *et al.*, Phys. Rev. Lett. **124**, 084802 (2020).

[37] Y. Takagi, N. Iwata, E. d'Humieres, and Y. Sentoku, Phys. Rev. Res. **3**, 043140 (2021).